Engineering Analysis with Boundary Elements 34 (2010) 405–416

Contents lists available at ScienceDirect

Engineering Analysis with Boundary Elements

journal homepage: www.elsevier.com/locate/enganabound

Coupling the BEM/TBEM and the MFS for the numerical simulation of acoustic wave propagation

António Tadeu *, Julieta António, Igor Castro

CICC, Department of Civil Engineering, University of Coimbra, Rua Luís Reis Santos-Pólo II da Universidade, 3030-788 Coimbra, Portugal

ARTICLE INFO

Article history:
Received 29 May 2009
Accepted 19 November 2009
Available online 22 December 2009

Keywords:
Acoustic wave propagation
TBEM/MFS coupling
TBEM+BEM/MFS coupling
Acoustic barriers

ABSTRACT

The coupling of the boundary element method (BEM)/the traction boundary element method (TBEM) and the method of fundamental solutions (MFS) is proposed for the transient analysis of acoustic wave propagation problems in the presence of multi-inclusions to overcome the limitations posed by each method. The full domain is divided into sub-domains which are modeled using the BEM/TBEM and the MFS, and the sub-domains are coupled with the imposition of the required boundary conditions. The accuracy of the proposed algorithms, using different combinations of BEM/TBEM and MFS, is verified by comparing the solutions against reference solutions. The applicability of the proposed method is shown by simulating the acoustic behavior of a rigid acoustic screen in the vicinity of a dome and by computing the acoustic attenuation provided by a fluid-filled thin inclusion separating two railway tracks in an underground train station.

1. Introduction

The propagation of acoustic waves due to static and moving pressure sources has been studied intensively in the past few decades. These waves may be produced by vehicles in the presence of acoustic barriers, by speakers in acoustic rooms, by ultrasound devices in the presence of cracks and inclusions and by acoustic logging tools inside boreholes. During this time some significant technical advances have been made, and our understanding of how waves propagate and radiate in elastic and acoustic media has improved, especially when the wave propagation process is linearly elastic and the solid is relatively homogenous.

Analytical solutions are only known for very simple geometric and material conditions such as circular cylindrical inclusions, homogeneous full spaces and half-spaces subjected to line loads and point loads of constant amplitude and infinite duration. The superposition of Green's functions (fundamental solutions) can be used for more complex situations like layered media. The resulting integral expressions are so complex, however, that they can only be evaluated by numerical means, and in general they require great computational effort.

The modeling of practical engineering acoustic vibration problems is usually quite difficult and several numerical methods of varying complexity have been developed (e.g. the thin layer method (TLM) [1], boundary element method (BEM) [2], the finite element method (FEM) [3,4], the finite difference method [5], the ray tracing technique [6]).

Of these techniques the BEM is one of the most suitable for modeling homogeneous unbounded systems containing irregular interfaces and inclusions since the far field conditions are automatically satisfied and only the boundaries of the interfaces and inclusions need to be discretized. Despite the fact that the BEM requires only boundary meshing it still needs prior knowledge of fundamental solutions, i.e. Green's functions. Its efficiency also depends on the correct integration of the singular and hypersingular integrals. In addition, for a certain level of accuracy, the number of boundary elements depends on the excitation frequency, requiring the use of many boundary elements to model high frequency responses. This leads to an undesirably high computational cost. Furthermore, the BEM tends to break down when applied to cracks and very thin heterogeneities [7]. The traction boundary element method (TBEM) is one numerical method that solves the thin-body difficulties that arise when modeling wave propagation in the presence of very thin heterogeneities such as small imperfections, dimensionless cracks or almost imperceptible defects.

The appearance of hypersingular integrals is one of the difficulties posed by these formulations. Different attempts have been made to overcome this difficulty [8–10]. Most of the work published refers to 2D geometries and, in some cases, 3D geometries. Amado Mendes and Tadeu [11] solved the case of a 2D empty crack buried in an unbounded medium subjected to a

* Corresponding author. Tel.: +351 239 797 100; fax: +351 239 797 123.
E-mail addresses: tadeu@dec.uc.pt (A. Tadeu), julieta@dec.uc.pt (J. António), igorasc@itecons.uc.pt (I. Castro).

0955-7997/$ - see front matter © 2009 Elsevier Ltd. All rights reserved.
doi:10.1016/j.enganabound.2009.11.003

3D source. The solution requires the application of a spatial Fourier transform along the direction in which the geometry of the crack does not vary. Thus, the 3D solution is obtained as a summation of 2D solutions for different spatial wavenumbers. The resulting hypersingular kernels were computed analytically by defining the dynamic equilibrium of semi-cylinders above the boundary elements that discretize the crack. That work extended the work by Prosper and Kausel [12] who defined the behavior of a 2D flat horizontal crack. Following that, Tadeu et al. [13] proposed a combined (or dual) BEM/TBEM formulation able to solve the case of fluid-filled thin inclusions placed in an unbounded medium, and in [14] they applied the same numerical techniques to the case of elastic scattering produced by thin rigid inclusions.

A frequency domain TBEM formulation has been presented by Tadeu et al. [15] and used to study the behavior of rigid acoustic screens attached to a tall building, and excited by a pressure/acoustic load. The model uses Green's functions that take into account the presence of the tall building's façade and a rigid floor, therefore making their discretization unnecessary. Using a similar technique, the 3D wave propagation around 2D rigid acoustic screens, with thickness approaching zero and placed in a fluid layer was studied by António et al. [16].

Another fairly common strategy is to formulate the problem using solid, finite elements, ideally with absorbing boundaries of some kind such as paraxial boundaries, or the rather effective transition elements obtained with the perfectly matched layer technique (PML). Finite elements have the added advantage that one can also model nonlinear effects near the load. However, the finite element method (FEM) requires the full discretization of the medium being analyzed. Unfortunately the FEM is computationally infeasible for very large scale models unless we take substantial short-cuts, by allowing coarse elements, restricting models to low frequencies, or tolerating boundary artifacts, not to mention neglecting the inherent nonlinearity of soils near the loads.

A different class of numerical techniques has become popular recently: the so-called meshless techniques that require neither domain nor boundary discretization [17–22]. The method of fundamental solutions (MFS) seems to be particularly effective for studying wave propagation since it overcomes some of the mathematical complexity of the BEM and provides acceptable solutions at substantially lower computational cost. Godinho et al. [23] studied the performance of the MFS for simulating the propagation of acoustic waves in a fluid domain with an inclusion. The authors concluded that the method can be very efficient, even outperforming the BEM for this type of problem. Godinho et al. [24] subsequently successfully employed the MFS to study acoustic and elastic wave propagation around thin structures using a domain decomposition technique. The MFS has been used more recently to simulate ground rotations along 2D topographical profiles under the incidence of elastic plane waves [25]. Other authors have proposed the use of enrichment functions to model torsional problems, including cracks [26].

Still, the use of the MFS has its own shortcomings and limitations in the presence of thin inclusions and inclusions with twisting (sinuous) boundaries. This work addresses the coupling of the BEM/TBEM and the MFS to overcome some of the limitations posed by each method.

The boundary element method (BEM)/traction boundary element (TBEM) and the method of fundamental solutions (MFS) are coupled for the transient analysis of acoustic wave propagation problems in the presence of multi-inclusions. The full domain is divided into sub-domains which are modeled using the BEM/TBEM and the MFS, and the sub-domains are coupled with the required boundary conditions being imposed. The approach is implemented for general 2D problems. In order to investigate the accuracy of the proposed coupling algorithms, using different combinations of BEM/TBEM and MFS formulations, a verification analysis is performed using reference solutions.

The problem is defined in the next section, and then the BEM/TBEM and MFS acoustic coupling formulations are established when multi-inclusions are submerged in an unbounded fluid medium. The coupling formulations are first verified against solutions obtained using BEM or MFS formulations, used as reference solutions. A brief section then describes how responses in the time domain are obtained by means of the fast inverse Fourier transformation, using a Ricker pulse as the excitation dynamic wavelet source. Finally, the applicability of the proposed method is shown by means of two numerical examples. In the first, the TBEM/MFS coupling algorithm is used to obtain the sound pressure attenuation provided by a null-thickness rigid acoustic barrier placed between an acoustic source and a dome. In the second, the BEM+TBEM/MFS coupling algorithm computes the scattered wavefield in the time domain produced by a thin acoustic barrier placed in an underground station, when illuminated by the pressure elicited by an acoustic source.

2. Boundary integral coupling formulations

Consider two two-dimensional irregular cylindrical inclusions, submerged in a spatially uniform fluid medium 1 with density ρ_1 (Fig. 1). This system is subjected to a harmonic point pressure source at O (x_s, y_s), which oscillates with a frequency ω, and originates an incident pressure at (x, y),

$$p_{inc}(x, y, \omega) = AH_0(k_{\alpha_1} r_1) \tag{1}$$

where the subscript *inc* represents the incident field, $r_1 = \sqrt{(x-x_s)^2+(y-y_s)^2}$, A the wave amplitude, $k_{\alpha_1} = (\omega/\alpha_1)$, α_1 the pressure wave velocity of the fluid medium, and $H_n(\ldots)$ correspond to second Hankel functions of order n. The fluid media 2 and 3 inside inclusions 1 and 2 have densities ρ_2, and ρ_3 and allow pressure wave velocities α_2 and α_3, respectively.

2.1. BEM/MFS coupling formulation

This section describes the coupling between the BEM and the MFS formulations used to obtain the two-dimensional pressure field generated by a pressure point source placed in the vicinity of, but outside, the two submerged inclusions with irregular shapes. One of the inclusions is modeled using the BEM while the other is solved with the MFS. Three types of inclusions will be modeled: fluid-filled inclusions, cavities with null pressures and rigid inclusions with null pressure gradients prescribed along their boundary.

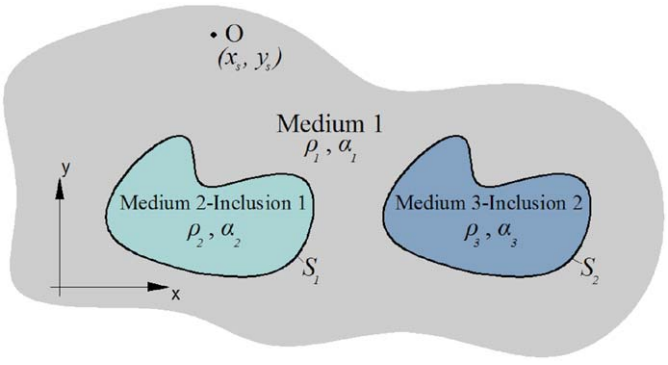

Fig. 1. Sketch of the geometry of the problem.

2.1.1. Fluid-filled inclusions

The pressure (p) at any point of the spatial domain can be calculated using the Helmoltz equation

$$\nabla^2 p(x,y,\omega)+(k_\alpha)^2 p(x,y,\omega)=0, \tag{2}$$

where $\nabla^2=\left(\frac{\partial^2}{\partial x^2}+\frac{\partial^2}{\partial y^2}\right)$.

Considering a host homogeneous fluid medium containing fluid inclusion 1, bounded by a surface S_1, and subjected to an incident pressure field given by p_{inc}, the boundary integral equation can be constructed by applying the reciprocity theorem (e.g. Manolis and Beskos [27]) leading to

a) in the exterior domain of inclusion 1 (Medium 1)

$$\begin{aligned} cp^{(1)}(x_0,y_0,\omega) &= \int_{S_1} q^{(1)}(x,y,\boldsymbol{n_{n1}},\omega)G^{(1)}(x,y,x_0,y_0,\omega)ds \\ -\int_{S_1} H^{(1)}(x,y,\boldsymbol{n_{n1}},x_0,y_0,\omega)p^{(1)}(x,y,\omega)ds &+ p_{inc}(x_0,y_0,x_s,y_s,\omega). \end{aligned} \tag{3}$$

In these equations, the superscript 1 corresponds to the exterior domain; $\boldsymbol{n_{n1}}$ is the unit outward normal along the boundary S_1; G and H are, respectively, the fundamental solutions (Green's functions) for the pressure (p) and pressure gradient (q), at (x,y) due to a virtual point pressure load at (x_0, y_0). p_{inc} is the pressure incident field at (x_0, y_0), when the point pressure source is located at (x_s, y_s). The factor c is a constant defined by the shape of the boundary, taking the value 1/2 if $(x_0,y_0)\in S_1$ and S_1 is smooth.

Eq. (3) does not yet take into account the presence of the neighboring inclusion 2, which is modeled using the MFS. The MFS assumes that the response of this neighboring inclusion is found as a linear combination of fundamental solutions simulating the pressure field generated by two sets of *NS* virtual sources. These virtual loads are distributed along the inclusion interface at distances δ from that boundary towards the interior and exterior of the inclusion (lines $\hat{C}^{(1)}$ and $\hat{C}^{(2)}$ in Fig. 2) in order to avoid singularities. Sources inside the inclusion have unknown amplitudes $a^{(2)}_{n\_ext}$, while those placed outside the inclusion have unknown amplitudes $a^{(2)}_{n\_int}$. In the exterior and interior fluid medium, the scattered pressure fields are given by

$$p^{(1)}(x,y,\omega)=\sum_{n=1}^{NS}\left[a^{(2)}_{n\_ext}G^{(1)}(x,y,x_{n\_ext},y_{n\_ext},\omega)\right]$$

$$p^{(3)}(x,y,\omega)=\sum_{n=1}^{NS}\left[a^{(2)}_{n\_int}G^{(3)}(x,y,x_{n\_int},y_{n\_int},\omega)\right], \tag{4}$$

where $G^{(1)}(x,y,x_{n\_ext},y_{n\_ext},\omega)$ and $G^{(3)}(x,y,x_{n\_int},y_{n\_int},\omega)$ are the fundamental solutions which represent the pressures at points (x, y) in mediums 1 and 3, generated by pressure loads acting at positions (x_{n_ext}, y_{n_ext}) and (x_{n_int}, y_{n_int}). *n_ext* and *n_int* are the subscripts that denote the load order number placed along lines $\hat{C}^{(1)}$ and $\hat{C}^{(2)}$, respectively.

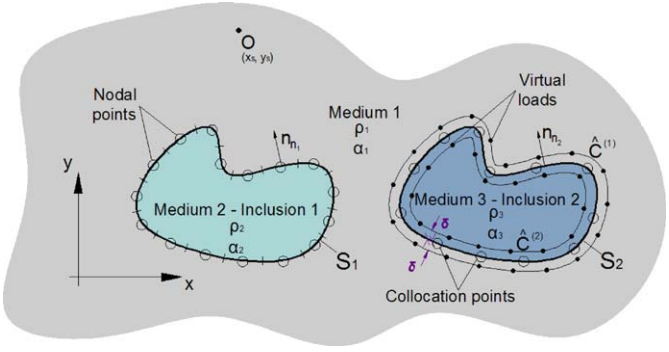

Fig. 2. Discretization of the system: position of virtual loads, collocation points and boundary elements.

The pressure field generated by this second inclusion can be viewed as an incident field that strikes the first inclusion. So Eq. (3) needs to be modified accordingly

$$\begin{aligned} cp^{(1)}(x_0,y_0,\omega) &= \int_{S_1} q^{(1)}(x,y,\boldsymbol{n_{n1}},\omega)G^{(1)}(x,y,x_0,y_0,\omega)ds \\ &-\int_{S_1} H^{(1)}(x,y,\boldsymbol{n_{n1}},x_0,y_0,\omega)p^{(1)}(x,y,\omega)ds+p_{inc}(x_0,y_0,x_s,y_s,\omega) \\ &+\sum_{n=1}^{NS}\left[a^{(2)}_{n\_ext}G^{(1)}(x_0,y_0,x_{n\_ext},y_{n\_ext},\omega)\right] \end{aligned} \tag{5}$$

b) in the interior domain of inclusion 1 (Medium 2)

$$\begin{aligned} cp^{(2)}(x_0,y_0,\omega) &= \int_{S_1} q^{(2)}(x,y,-\boldsymbol{n_{n1}},\omega)G^{(2)}(x,y,x_0,y_0,\omega)ds \\ &-\int_{S_1} H^{(2)}(x,y,-\boldsymbol{n_{n1}},x_0,y_0,\omega)p^{(2)}(x,y,\omega)ds. \end{aligned} \tag{6}$$

In Eq. (6), the superscript 2 corresponds to the domain inside inclusion 1.

c) in the interior and exterior domain of inclusion 2 (Mediums 1 and 3)

To determine the amplitudes of the unknown virtual pressure loads $a^{(2)}_{n\_ext}$ and $a^{(2)}_{n\_int}$, it is also necessary to impose the continuity of pressures and normal pressure gradients at interface S_2, which is the boundary of inclusion 2, along *NS* collocation points (x_{col},y_{col}). This must be done taking into account the scattered field generated at inclusion 1. Thus the following two equations are defined:

$$\begin{aligned} &\int_{S_1} q^{(1)}(x,y,\boldsymbol{n_{n1}},\omega)G^{(1)}(x,y,x_{col},y_{col},\omega)ds \\ &-\int_{S_1} H^{(1)}(x,y,\boldsymbol{n_{n1}},x_{col},y_{col},\omega)p^{(1)}(x,y,\omega)ds+p_{inc}(x_{col},y_{col},x_s,y_s,\omega) \\ &+\sum_{n=1}^{NS}\left[a^{(2)}_{n\_ext}G^{(1)}(x_{col},y_{col},x_{n\_ext},y_{n\_ext},\omega)\right] \\ &=\sum_{n=1}^{NS}\left[a^{(2)}_{n\_int}G^{(3)}(x_{col},y_{col},x_{n\_int},y_{n\_int},\omega)\right], \end{aligned} \tag{7}$$

$$\begin{aligned} &\int_{S_1} q^{(1)}(x,y,\boldsymbol{n_{n1}},\omega)\frac{\partial G^{(1)}}{\partial \boldsymbol{n_{n2}}}(x,y,\boldsymbol{n_{n2}},x_{col},y_{col},\omega)ds \\ &-\int_{S_1}\frac{\partial H^{(1)}}{\partial \boldsymbol{n_{n2}}}(x,y,\boldsymbol{n_{n1}},\boldsymbol{n_{n2}},x_{col},y_{col},\omega)p^{(1)}(x,y,\omega)ds \\ &+\frac{\partial p_{inc}}{\partial \boldsymbol{n_{n2}}}(x_{col},y_{col},\boldsymbol{n_{n2}},x_s,y_s,\omega) \\ &+\sum_{n=1}^{NS}\left[a^{(2)}_{n\_ext}\frac{\partial G^{(1)}}{\partial \boldsymbol{n_{n2}}}(x_{col},y_{col},\boldsymbol{n_{n2}},x_{n\_ext},y_{n\_ext},\omega)\right] \\ &=\sum_{n=1}^{NS}\left[a^{(2)}_{n\_int}\frac{\rho_1}{\rho_3}\frac{\partial G^{(3)}}{\partial \boldsymbol{n_{n2}}}(x_{col},y_{col},\boldsymbol{n_{n2}},x_{n\_int},y_{n\_int},\omega)\right] \end{aligned} \tag{8}$$

In these equations, $\boldsymbol{n_{n2}}$ is the unit outward normal to the boundary S_2.

d) Final system of equations

The global solution is obtained by solving Eqs. (5–8). This requires the discretization of the interface S_1, which is the boundary of inclusion 1. Throughout this work this interface is discretized into N straight boundary elements, with one nodal point in the middle of each element (see Fig. 2).

The required two-dimensional Green's functions for pressure and pressure gradients in Cartesian co-ordinates are those for an unbounded solid medium

$$G^{(m)}(x,y,x_k,y_k,\omega)=-(i/4)H_0(k_{\alpha_m}r) \tag{9}$$

$$H^{(m)}(x,y,\boldsymbol{n_{n1}},x_k,y_k,\omega)=(i/4)k_{\alpha_m}H_1(k_{\alpha_m}r)\frac{\partial r}{\partial \boldsymbol{n_{n1}}} \tag{10}$$

$$\frac{\partial G^{(m)}}{\partial \boldsymbol{n}_{\boldsymbol{n2}}}(x,y,\boldsymbol{n}_{\boldsymbol{n2}},x_k,y_k,\omega)=(i/4)k_{\alpha_m}H_1\left(k_{\alpha_m}r\right)\frac{\partial r}{\partial \boldsymbol{n}_{\boldsymbol{n2}}} \tag{11}$$

$$\begin{aligned}\frac{\partial H^{(m)}}{\partial \boldsymbol{n}_{\boldsymbol{n2}}}(x,y,\boldsymbol{n}_{\boldsymbol{n1}},\boldsymbol{n}_{\boldsymbol{n2}},x_k,y_k,\omega)=&\\ (i/4)k_{\alpha_m}\left\{\left[\frac{1}{r}H_1\left(k_{\alpha_m}r\right)-k_{\alpha_m}H_2\left(k_{\alpha_m}r\right)\right]\frac{\partial r}{\partial \boldsymbol{n}_{\boldsymbol{n1}}}\frac{\partial r}{\partial \boldsymbol{n}_{\boldsymbol{n2}}}+\frac{H_1\left(k_{\alpha_m}r\right)}{r}\right.&\\ \times\left[\left(\frac{\partial r}{\partial y}\right)^2\frac{\partial x}{\partial \boldsymbol{n}_{\boldsymbol{n1}}}\frac{\partial x}{\partial \boldsymbol{n}_{\boldsymbol{n2}}}-\frac{\partial r}{\partial y}\frac{\partial r}{\partial x}\left(\frac{\partial x}{\partial \boldsymbol{n}_{\boldsymbol{n1}}}\frac{\partial y}{\partial \boldsymbol{n}_{\boldsymbol{n2}}}+\frac{\partial x}{\partial \boldsymbol{n}_{\boldsymbol{n2}}}\frac{\partial y}{\partial \boldsymbol{n}_{\boldsymbol{n1}}}\right)\right.&\\ \left.\left.+\left(\frac{\partial r}{\partial x}\right)^2\frac{\partial y}{\partial \boldsymbol{n}_{\boldsymbol{n1}}}\frac{\partial y}{\partial \boldsymbol{n}_{\boldsymbol{n2}}}\right]\right\},&\end{aligned} \tag{12}$$

in which $r=\sqrt{(x-x_k)^2+(y-y_k)^2}$. The pressure wave velocities in these equations are the ones associated with the exterior and the interior fluid of the inclusions ($m=1,2$).

The required integrations in Eqs. (5–8) are evaluated using a Gaussian quadrature scheme when they are not performed along the loaded element. For the loaded element, the existing singular integrands in the source terms of the Green's functions are calculated analytically, following the expressions in Tadeu et al. [28],

$$\begin{aligned}\int_0^{L/2}H_0(k_\alpha r)dr=&\frac{L}{2}H_0\left(k_\alpha\frac{L}{2}\right)+\pi\frac{L}{4}\left[H_1\left(k_\alpha\frac{L}{2}\right)S_0\left(k_\alpha\frac{L}{2}\right)\right.\\ &\left.-H_0\left(k_\alpha\frac{L}{2}\right)S_1\left(k_\alpha\frac{L}{2}\right)\right],\end{aligned} \tag{13}$$

where $S_{ns}(\ldots)$ are Struve functions of order ns and L the boundary element length.

The final integral equations are manipulated and combined so as to impose the continuity of pressure and pressure gradients along the boundary of the inclusions 1 and 2, to establish a system of $[(2NS+2N)\times(2NS+2N)]$ equations,

$$\begin{bmatrix} G^{(1)kl} & -H^{(1)kl} & G_p^{(1)kn} & 0\\ -\dfrac{\rho_2}{\rho_1}G^{(2)kl} & -H^{(2)kl} & 0 & 0\\ G^{(1)nl} & -H^{(1)nl} & G_p^{(1)nn} & -G_p^{(3)nn}\\ \dfrac{\partial G^{(1)nl}}{\partial \boldsymbol{n}_{\boldsymbol{n2}}} & -\dfrac{\partial H^{(1)nl}}{\partial \boldsymbol{n}_{\boldsymbol{n2}}} & \dfrac{\partial G_p^{(1)nn}}{\partial \boldsymbol{n}_{\boldsymbol{n2}}} & -\dfrac{\rho_1}{\rho_3}\dfrac{\partial G_p^{(3)nn}}{\partial \boldsymbol{n}_{\boldsymbol{n2}}} \end{bmatrix}\begin{bmatrix} q^{(1)l}\\ p^{(1)l}\\ a^n_{n\_ext}\\ a^n_{n\_\mathrm{int}}\end{bmatrix}=\begin{bmatrix} -p^k_{inc}\\ 0\\ -p^n_{inc}\\ -\dfrac{\partial p^n_{inc}}{\partial \boldsymbol{n}_{\boldsymbol{n2}}}\end{bmatrix}, \tag{14}$$

where $k,l=1,N$, $n=1,NS$, l identifies the element being integrated,

$$G^{(m)km}=\int_{C_l}G^{(m)}(x_l,y_l,x_k,y_k,\omega)dC_l,\ H^{(m)kl}=\int_{C_l}H^{(m)}(x_l,y_l,\boldsymbol{n}_{\boldsymbol{n1}},x_k,y_k,\omega)dC_l,$$
$$G^{(1)nl}=\int_{C_l}G^{(1)}(x_l,y_l,x_n,y_n,\omega)dC_l,\ H^{(1)nl}=\int_{C_l}H^{(1)}(x_l,y_l,\boldsymbol{n}_{\boldsymbol{n1}},x_n,y_n,\omega)dC_l,$$
$$G_p^{(1)kn}=G^{(1)}(x_k,y_k,x_{n\_ext},y_{n\_ext},\omega),\ G_p^{(1)nn}=G^{(1)}(x_n,y_n,x_{n\_ext},y_{n\_ext},\omega),$$
$$G_p^{(3)nn}=G^{(3)}(x_n,y_n,x_{n\_int},y_{n\_int},\omega).$$

The solution of this system of equations gives the nodal pressures and pressure gradients along the boundary S_1 and the unknown virtual pressure load amplitudes, $a^{(2)}_{n\_ext}$ and $a^{(2)}_{n\_int}$, which allow the pressure field to be defined inside and outside the inclusions.

2.1.2. Rigid inclusions (null pressure gradients along their boundaries)

In this case, the boundary conditions prescribe null normal pressure gradients along the boundary S. Thus, Eqs. (5–8) are simplified to

$$\begin{aligned}cp^{(1)}(x_0,y_0,\omega)=&\\ -\int_{S_1}H^{(1)}(x,y,\boldsymbol{n}_{\boldsymbol{n1}},x_0,y_0,\omega)p^{(1)}(x,y,\omega)ds+p_{inc}(x_0,y_0,x_s,y_s,\omega)&\\ +\sum_{n=1}^{NS}\left[a^{(2)}_{n\_ext}G^{(1)}(x_0,y_0,x_{n\_ext},y_{n\_ext},\omega)\right],&\end{aligned} \tag{15}$$

$$\begin{aligned}&-\int_{S_1}\frac{\partial H^{(1)}}{\partial \boldsymbol{n}_{\boldsymbol{n2}}}(x,y,\boldsymbol{n}_{\boldsymbol{n1}},\boldsymbol{n}_{\boldsymbol{n2}},x_{col},y_{col},\omega)p^{(1)}(x,y,\omega)ds\\ &+\frac{\partial p_{inc}}{\partial \boldsymbol{n}_{\boldsymbol{n2}}}(x_{col},y_{col},\boldsymbol{n}_{\boldsymbol{n2}},x_s,y_s,\omega)\\ &+\sum_{n=1}^{NS}\left[a^{(2)}_{n\_ext}\frac{\partial G^{(1)}}{\partial \boldsymbol{n}_{\boldsymbol{n2}}}(x_{col},y_{col},\boldsymbol{n}_{\boldsymbol{n2}},x_{n\_ext},y_{n\_ext},\omega)\right]=0\end{aligned} \tag{16}$$

The solution of this integral for the boundary surface (S_1) again requires the discretization of the boundary of inclusion 1 into N straight boundary elements and the simulation of inclusion 2 using NS collocation points/virtual sources. The procedure is similar to the one described above and leads to a system of $[(NS+N)\times(NS+N)]$ equations.

2.1.3. Cavity inclusions (null pressures along their boundaries)

Null pressures are now prescribed on the surface of the cavities, which leads to the equations

$$\begin{aligned}&\int_{S_1}q^{(1)}(x,y,\boldsymbol{n}_{\boldsymbol{n1}},\omega)G^{(1)}(x,y,x_0,y_0,\omega)ds+p_{inc}(x_0,y_0,x_s,y_s,\omega)\\ &\quad+\sum_{n=1}^{NS}\left[a^{(2)}_{n\_ext}G^{(1)}(x_0,y_0,x_{n\_ext},y_{n\_ext},\omega)\right]=0,\end{aligned} \tag{17}$$

$$\begin{aligned}&\int_{S_1}q^{(1)}(x,y,\boldsymbol{n}_{n1},\omega)G^{(1)}(x,y,x_{col},y_{col},\omega)ds\\ &+p_{inc}(x_{col},y_{col},x_s,y_s,\omega)+\sum_{n=1}^{NS}\left[a^{(2)}_{n\_ext}G^{(1)}(x_{col},y_{col},x_{n\_ext},y_{n\_ext},\omega)\right]=0\end{aligned} \tag{18}$$

The solution of this equation is once again obtained using the procedure described before. Other combinations of inclusions can be solved by simplifying Eqs. (5–8) according to the required boundary conditions.

2.2. TBEM/MFS coupling formulation

The traction boundary element method (TBEM) can be formulated as for the case of fluid-filled thin inclusions in an elastic medium [29], leading to the following Eqs. (19–20) that replace the former Eqs. (5–6), while modeling the first inclusion

$$\begin{aligned}&ap^{(1)}(x_0,y_0,\omega)+cq^{(1)}(x_0,y_0,\boldsymbol{n}_{\boldsymbol{n1}},\omega)\\ &\quad=\int_{S_1}q^{(1)}(x,y,\boldsymbol{n}_{\boldsymbol{n1}},\omega)\overline{G}^{(1)}(x,y,\boldsymbol{n}_{\boldsymbol{n2}},x_0,y_0,\omega)ds\\ &\quad-\int_{S_1}\overline{H}^{(1)}(x,y,\boldsymbol{n}_{\boldsymbol{n1}},\boldsymbol{n}_{\boldsymbol{n2}},x_0,y_0,\omega)p^{(1)}(x,y,\omega)ds\\ &\quad+\overline{p}_{inc}(x_0,y_0,\boldsymbol{n}_{\boldsymbol{n2}},x_s,y_s,\omega)\\ &\quad+\sum_{n=1}^{NS}\left[a^{(2)}_{n\_ext}\overline{G}^{(1)}(x_0,y_0,\boldsymbol{n}_{\boldsymbol{n2}},x_{n\_ext},y_{n\_ext},\omega)\right],\end{aligned} \tag{19}$$

$$\begin{aligned}&ap^{(2)}(x_0,y_0,\omega)+cq^{(2)}(x_0,y_0,\boldsymbol{n}_{\boldsymbol{n1}},\omega)\\ &=\int_{S_1}q^{(2)}(x,y,\boldsymbol{n}_{\boldsymbol{n1}},\omega)\overline{G}^{(2)}(x,y,\boldsymbol{n}_{\boldsymbol{n2}},x_0,y_0,\omega)ds\\ &\int_{S_1}\overline{H}^{(2)}(x,y,\boldsymbol{n}_{\boldsymbol{n1}},\boldsymbol{n}_{\boldsymbol{n2}},x_0,y_0,\omega)p^{(2)}(x,y,\omega)ds.\end{aligned} \tag{20}$$

Eqs. (7) and (8) can be kept the same. Eqs. (19) and (20) can be seen to result from the application of dipoles (*dynamic doublets*) along the boundary surface (S_1). As noted by Guiggiani [30] the coefficient a is zero for piecewise straight boundary elements. The factor c is a constant defined as above.

The solutions of these equations are defined as before by discretizing the boundary surface (S_1) into N straight boundary elements, with one nodal point in the middle of each element. The required two-dimensional Green's functions are now defined as

$$\overline{G}^{(m)}(x,y,\boldsymbol{n_k},x_k,y_k,\omega)=(i/4)k_\alpha H_1(k_{\alpha_m}r)\frac{\partial r}{\partial \boldsymbol{n_k}}, \tag{21}$$

$$\begin{aligned}\overline{H}^{(m)}&(x,y,\boldsymbol{n_l},\boldsymbol{n_k},x_k,y_k,\omega)\\ &=\frac{i}{4}k_{\alpha m}\left\{-k_{\alpha m}H_2(k_{\alpha m}r)\left[\left(\frac{\partial r}{\partial x}\right)^2\frac{\partial x}{\partial \boldsymbol{n_l}}+\frac{\partial r}{\partial x}\frac{\partial r}{\partial y}\frac{\partial y}{\partial \boldsymbol{n_l}}\right]\right.\\ &\left.+\frac{H_1(k_{\alpha m}r)}{r}\left[\frac{\partial x}{\partial \boldsymbol{n_l}}\right]\right\}\frac{\partial x}{\partial \boldsymbol{n_k}}+\frac{i}{4}k_{\alpha m}\left\{-k_{\alpha m}H_2(k_{\alpha m}r)\left[\frac{\partial r}{\partial x}\frac{\partial r}{\partial y}\frac{\partial x}{\partial \boldsymbol{n_l}}\right.\right.\\ &\left.\left.+\left(\frac{\partial r}{\partial y}\right)^2\frac{\partial y}{\partial \boldsymbol{n_l}}\right]+\frac{H_1(k_{\alpha m}r)}{r}\left[\frac{\partial y}{\partial \boldsymbol{n_l}}\right]\right\}\frac{\partial y}{\partial \boldsymbol{n_k}},\end{aligned} \tag{22}$$

where $\boldsymbol{n}_k$ and $\boldsymbol{n}_l$ are the unit outward normals to the boundary segments being loaded and integrated, respectively. In Eq. (19) the incident field is computed as

$$\overline{p}_{inc}(x,y,\boldsymbol{n_k},x_s,y_s,\omega)=\frac{iA}{2}k_\alpha H_1(k_\alpha r_1)\left(\frac{x-x_s}{r_1}\frac{\partial x}{\partial \boldsymbol{n_k}}+\frac{y-y_s}{r_1}\frac{\partial y}{\partial \boldsymbol{n_k}}\right). \tag{23}$$

The integrations in Eqs. (19) and (20) are performed through a Gaussian quadrature scheme when the element being integrated is not the loaded one. When the element being integrated (C_l) is the loaded one, the following integral becomes hypersingular:

$$\begin{aligned}\int_{C_l}\overline{H}^{(m)}&(x,y,\boldsymbol{n_l},\boldsymbol{n_l},x_k,y_k,\omega)dC_l\\ &=\int_{C_l}\frac{i}{4}k_{\alpha m}\left[-k_\alpha H_2(k_{\alpha m}r)\left(\frac{\partial r}{\partial x}\frac{\partial x}{\partial \boldsymbol{n_l}}+\frac{\partial r}{\partial y}\frac{\partial y}{\partial \boldsymbol{n_l}}\right)^2+\frac{H_1(k_{\alpha m}r)}{r}\right]dC_l.\end{aligned} \tag{24}$$

This integral can be evaluated analytically, considering the dynamic equilibrium of a semi-cylinder bounded by the boundary element, leading to

$$\begin{aligned}\int_{C_l}\overline{H}^{(m)}&(x,y,\boldsymbol{n_l},\boldsymbol{n_l},x_k,y_k,\omega)dC_l\\ &=\frac{i}{2}(k_{\alpha m})^2\left[\int_0^{L/2}H_0(k_{\alpha m}r)dr-\frac{1}{k_{\alpha m}}H_1\left(k_{\alpha m}\frac{L}{2}\right)\right],\end{aligned} \tag{25}$$

where L stands for the length of the boundary element. The integral $\int_0^{L/2}H_0(k_{\alpha m}\ r)dr$ is evaluated as indicated above. The final system of equations is obtained by combining Eqs. (7,8), and Eqs. (19,20) and imposing the continuity of pressure and pressure gradients along the boundary of inclusions 1 and 2.

$$\begin{bmatrix}\overline{G}^{(1)kl} & -\overline{H}^{(1)kl} & \overline{G}_p^{(1)kn} & 0\\ -\frac{\rho_2}{\rho_1}\overline{G}^{(2)kl} & -\overline{H}^{(2)kl} & 0 & 0\\ G^{(1)nl} & -H^{(1)nl} & G_p^{(1)nn} & -G_p^{(3)nn}\\ \frac{\partial G^{(1)nl}}{\partial \boldsymbol{n_{n2}}} & -\frac{\partial H^{(1)nl}}{\partial \boldsymbol{n_{n2}}} & \frac{\partial G_p^{(1)nn}}{\partial \boldsymbol{n_{n2}}} & -\frac{\rho_1}{\rho_3}\frac{\partial G_p^{(3)nn}}{\partial \boldsymbol{n_{n2}}}\end{bmatrix}\begin{bmatrix}q^{(1)l}\\ p^{(1)l}\\ a^n_{n\_ext}\\ a^n_{n\_\mathrm{int}}\end{bmatrix}=\begin{bmatrix}-\overline{p}^{k}_{inc}\\ 0\\ -p^n_{inc}\\ -\frac{\partial p^n_{inc}}{\partial \boldsymbol{n_{n2}}}\end{bmatrix}, \tag{26}$$

where $k,l=1, N$, $n=1, NS$,

$$\overline{G}^{(m)kl}=\int_{C_l}\overline{G}^{(m)}(x_l,y_l,\boldsymbol{n_{n_2}},x_k,y_k,\omega)dC_l,$$

$$\overline{H}^{(m)kl}=\int_{C_l}\overline{H}^{(m)}(x_l,y_l,\boldsymbol{n_{n1}},\boldsymbol{n_{n2}},x_k,y_k,\omega)dC_l,$$

$$\overline{G}_p^{(1)kn}=\overline{G}^{(1)}(x_k,y_k,\boldsymbol{n_{n_2}},x_{n\_ext},y_{n\_ext},\omega).$$

Manipulating Eqs. (7,8), and Eqs. (19,20), as described above, the cavity and the rigid inclusions can also be modeled.

The present TBEM formulation overcomes the thin-body difficulty, while the classical direct BEM formulation degenerates. The direct application of this method allows an empty or rigid crack to be modeled using a single open line representation. In the case of a rigid or empty submerged fissure the results identify the pressure or pressure gradient jumps between the two sides of the element.

2.3. Combined TBEM+BEM/MFS coupling formulation

The TBEM and BEM formulations can be combined so as to solve the same problems described above. However, it allows the solution to be defined when the inclusion 1 is a thin fluid-filled inclusion. Part of the boundary surface of that inclusion is loaded with monopole loads (BEM formulation), while the remaining part is loaded with dipoles (TBEM formulation). This leads to the following system of equations:

$$\begin{bmatrix}G^{(1)k_1l} & -H^{(1)k_1l} & G_p^{(1)k_1n} & 0\\ \overline{G}^{(1)k_2l} & -\overline{H}^{(1)k_2l} & \overline{G}_p^{(1)k_2n} & 0\\ -\frac{\rho_2}{\rho_1}G^{(2)k_1l} & -H^{(2)k_1l} & 0 & 0\\ -\frac{\rho_2}{\rho_1}\overline{G}^{(2)k_2l} & -\overline{H}^{(2)k_2l} & 0 & 0\\ G^{(1)nl} & -H^{(1)nl} & G_p^{(1)nn} & -G_p^{(3)nn}\\ \frac{\partial G^{(1)nl}}{\partial \boldsymbol{n_{n2}}} & -\frac{\partial H^{(1)nl}}{\partial \boldsymbol{n_{n2}}} & \frac{\partial G_p^{(1)nn}}{\partial \boldsymbol{n_{n2}}} & -\frac{\rho_1}{\rho_3}\frac{\partial G_p^{(3)nn}}{\partial \boldsymbol{n_{n2}}}\end{bmatrix}\begin{bmatrix}q^{(1)l}\\ p^{(1)l}\\ a^n_{n\_ext}\\ a^n_{n\_int}\end{bmatrix}=\begin{bmatrix}-p^{k_1}_{inc}\\ -\overline{p}^{k_2}_{inc}\\ 0\\ 0\\ -p^n_{inc}\\ -\frac{\partial p^n_{inc}}{\partial \boldsymbol{n_{n2}}}\end{bmatrix}, \tag{27}$$

with $k_1=1$, $(N/2)$, $k_2=(N/2)+1$, N, $l=1$, N, $n=1$, NS.

In this case the thin bodies can be solved using a closed surface. The empty or the rigid inclusions may exhibit zero thickness, and the pressure or pressure gradients are computed directly on both sides of the element.

3. Verification of the coupling algorithms

The proposed coupling algorithms (BEM/MFS, TBEM/MFS and combined BEM+TBEM/MFS) described are verified against BEM and MFS solutions by solving the scattered field produced by two circular inclusions, centered at (0.0, 20.0) and (20.0, 5.0), with radii between 5.0 and 4.0 m, respectively, submerged in an unbounded or half-space fluid medium. Five distinct problems are solved by combining different types of inclusion, viz. a fluid inclusion, a rigid inclusion and a cavity, according to Table 1.

The host fluid medium (ρ_1=4000 kg/m^3) is homogeneous, permitting a pressure wave velocity α_1=750 m/s. The fluid filling inclusions 1 and 2, with density ρ_2=2000 and ρ_3=3000 kg/m^3, exhibits a pressure wave velocity α_2=2121 and α_3=577 m/s, respectively. The system is excited by a harmonic point pressure load, applied at point O (3.0, 4.0 m), as in Fig. 3.

Table 1
Problems solved: types of inclusion and host medium.

	Inclusion 1	Inclusion 2	Host medium
Case 1	Fluid	Fluid	unbounded
Case 2	Rigid	Rigid	unbounded
Case 3	Cavity	Cavity	unbounded
Case 4	Fluid	Rigid	unbounded
Case 5	Rigid	Rigid	half-space

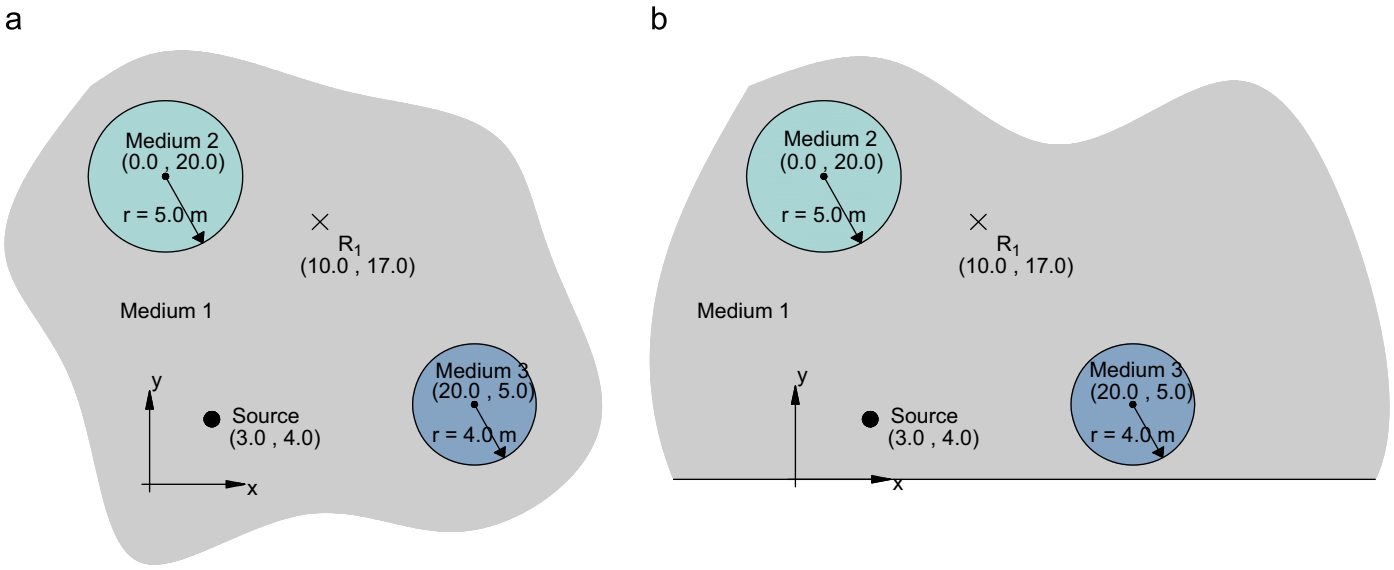

Fig. 3. Two circular inclusions in a homogeneous fluid medium: (a) unbounded medium; (b) half-space.

The pressure responses are computed for receiver R_1, placed at (10.0, 17.0 m). The computations are performed in the frequency domain in the range from 1 to 100Hz.

The computations are performed for different numbers of boundary elements and virtual sources in order to verify the consistency of results. The BEM/BEM results, using 120 boundary elements to model each inclusion are used as reference. Combinations of BEM/MFS, TBEM/MFS and MFS/MFS use different numbers of constant boundary elements and virtual sources. The distances between the virtual sources and the boundary have been determined by analyzing the errors along the boundary. The errors along the boundary interface were found by placing a set of receivers along the boundary, in addition to the collocation points used to solve the problem. The global boundary error is found by computing the integral error surface which is generated by the difference between the responses at these receivers and the prescribed boundary conditions. The distances finally adopted for the position of the virtual sources were those that led to the lowest boundary errors. All illustrated simulations used interior and exterior virtual sources placed respectively at distances $0.9\times r$ and $1.1.\times r$ from the centre of the inclusion.

The half-space coupling solutions (Case 5) are solved using half-space Green's functions. Thus, the Green's functions defined by Eq. (9) must be reformulated to satisfy the boundary conditions at the rigid ground, which require null normal pressure gradients. These conditions can be satisfied automatically by superposing the pressure field generated by the real source (placed at (x_k, y_k)) and the one elicited by a virtual source (image source), located in such a way that it constitutes a mirror in relation to the horizontal ground plane leading to a Green's function defined by Eq. (28). This mirror technique can be visualized as a superposition of the actual source and sound field reflected from the ground. Thus only the cross-sections of the inclusions need to be discretized.

The half-space Green's function is then expressed as

$$G^{(m)}_{half}(x,y,x_k,y_k,\omega) = -(i/4)\left[H_0\left(k_{\alpha_m} r_1\right) + H_0\left(k_{\alpha_m} r_2\right)\right], \tag{28}$$

in which $r_1 = \sqrt{(x-x_k)^2+(y-y_k)^2}$ and $r_2 = \sqrt{(x-x_k)^2+(y+y_k)^2}$ correspond to the distances between the receiver and the real and the virtual source, respectively.

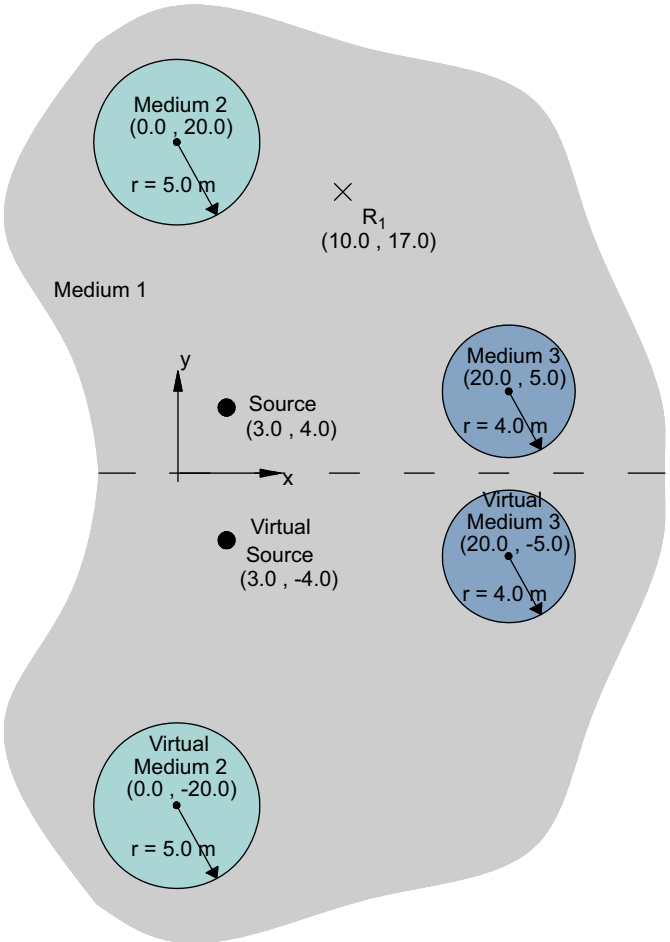

Fig. 4. Geometry used in the BEM model for Case 5.

The reference solution is provided by a BEM code that uses Green's functions for an unbounded medium. The geometry of the problem is thus built using the real inclusions and load, and its mirror images in relation to the horizontal plane x=0.0m (see Fig. 4).

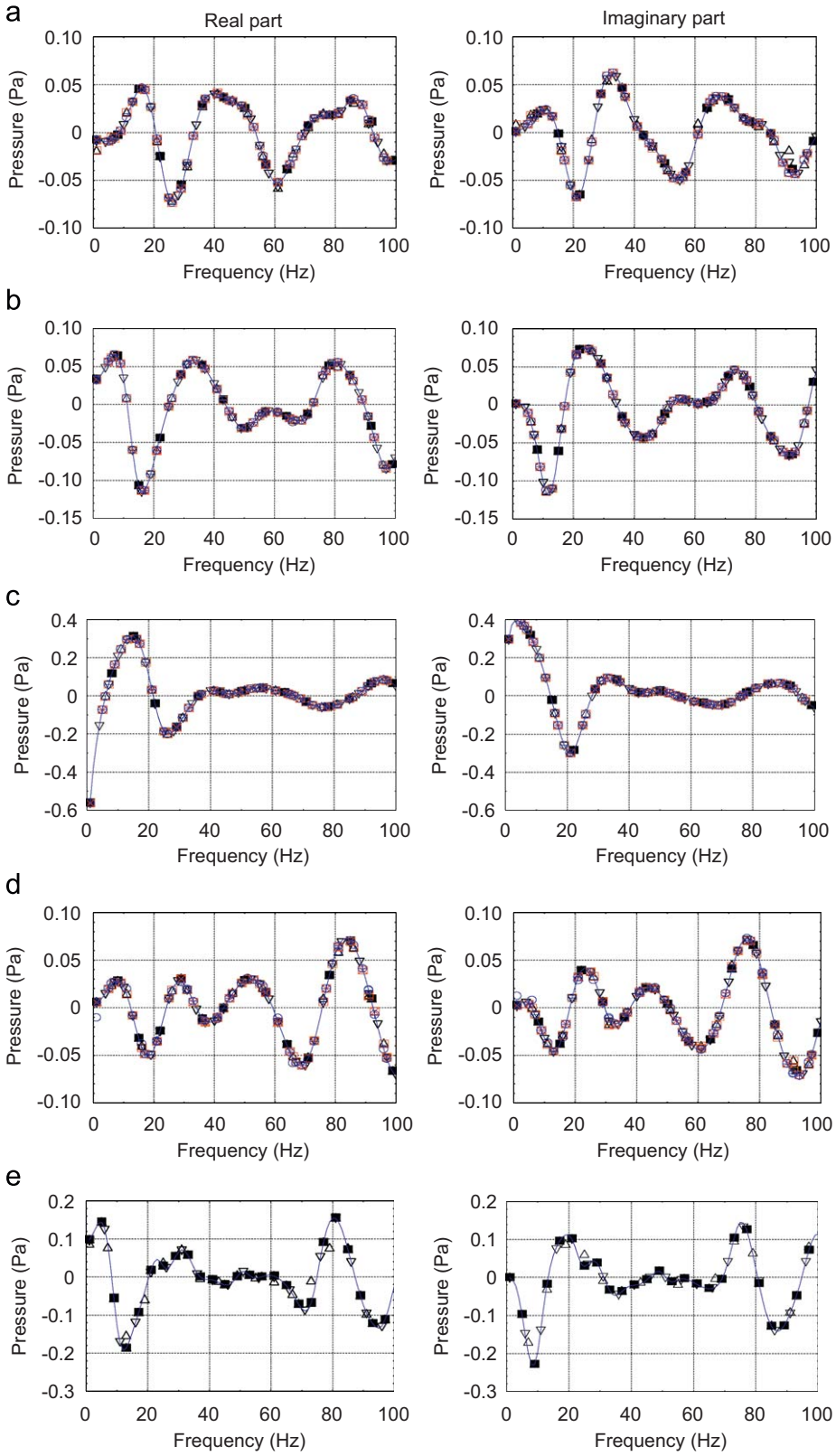

Fig. 5. BEM, MFS and coupling responses when the system is excited by a pressure load.— BEM/BEM (120/120); MFS/MFS (○ 40/40 ⊖ 80/80 ⊕ 120/120); BEM/MFS (□ 40/40 ⊟ 80/80 ⊠ 120/120) ; TBEM/MFS (△ 40/40 ▽ 80/80 ▲ 120/120): (a) Case 1; (b) Case 2; (c) Case 3; (d) Case 4; (e) Case 5.

Fig. 5 presents the real (left column) and imaginary (right column) parts of the pressure responses for cases 1–5. The lines correspond to the BEM responses (used here as reference solutions), that is, when both inclusions are modeled with 120 boundary elements, while the different MFS and coupling solutions are represented by the marked points and labeled "MFS/MFS", "BEM/MFS" and "TBEM/MFS". The numbers of boundary elements and virtual sources used in the coupling

solutions are 40, 80 and 120. An analysis of the results reveals that a very good agreement between the proposed coupling solutions and both the BEM and MFS models' solutions is reached, especially when the number of virtual sources and boundary elements is 120.

4. Pressure in time-space

Given that the computations are performed in the frequency domain, time responses in the space domain are computed by applying an inverse (Fast) Fourier Transform in ω, using a Ricker pulse as the dynamic excitation source, with temporal variation given by

$$u(\tau) = A(1-2\tau^2)e^{-\tau^2}, \tag{29}$$

where A represents the amplitude; and $\tau = (t-t_s)/t_0$, with t being the time, t_s, the time when the wavelet takes its maximum value, and πt_0 the characteristic (dominant) period of the Ricker wavelet.

The application of a Fourier transformation to this function, leads to

$$U(\omega) = A\left[2t_0\sqrt{\pi}e^{-i\omega t_s}\right]\ \Omega^2 e^{-\Omega^2}, \tag{30}$$

with $\Omega = \omega t_0/2$.

The Fourier transformation is computed by adding together a finite number of terms. This process corresponds to summing equally spaced sources with time intervals of $T=2\pi/\Delta\omega$. In these expressions the frequency increment is defined by $\Delta\omega$. It is essential that $\Delta\omega$ is small enough to avoid contaminating the response in the time domain (aliasing phenomena). This is almost eliminated by the introduction of complex frequencies with a small imaginary part of the form $\omega_c = \omega - i\eta$ (with $\eta = 0.7\Delta\omega$).

5. Applications

The applicability of the proposed coupling formulations is illustrated by solving two problems. The acoustic behavior of a rigid acoustic screen in the vicinity of a dome is addressed in the first example. The second example concerns the computation of the pressure field produced by a pressure source in an underground train station in the presence of a thin barrier that is modeled as a fluid-filled thin inclusion. The wave velocity allowed in the host medium and its density are kept constant and equal to 340 m/s and 1.22 kg/m^3, respectively.

The computations are performed in the frequency domain for frequencies ranging from 4 to 2048 Hz, with a frequency increment of 4 Hz, which determines a total time window for the analysis of 0.25 s.

5.1. Null-thickness rigid acoustic screen in the vicinity of a dome

A rigid acoustic screen, placed in a vicinity of a dome, is used to illustrate the capabilities of the proposed TBEM/MFS formulation. The pressure source is placed 4.0 m from the barrier in the horizontal direction, and 0.5 m above the ground, as Fig. 6 shows. The barrier, 3.0 m, tall, is placed 5.0 m from a semi-circular dome.

The pressure response is obtained over a two-dimensional grid of 26,347 receivers arranged along the x and y directions at equal intervals and placed in the vicinity of the acoustic barrier and dome from x=0.0 to 25.0 m and from y=0.0 to 10.0 m.

The barrier is modeled as a rigid screen using the TBEM. It has null-thickness and is discretized using an appropriate number of boundary elements defined by the relation between the wavelength and the length of the boundary elements, which was set at 6. A minimum of 30 boundary elements were used. The dome is assumed to be rigid and simulated by MFS, using a minimum of 200 virtual loads/collocation points. In the present example, the virtual loads are placed 0.5 m from its boundary. This distance was determined by using a procedure similar to that described previously in the verification section, based on the calculation of errors along the boundary. The number of virtual sources/collocation points increases with the frequency according to the relation between the wavelength and the distance between collocation points, which was set at 6.

Fig. 7 illustrates schematically the position of the virtual sources, collocation points and boundary elements. The problem uses adequate Green's functions for a half-space, taking into account the presence of a rigid ground floor.

The source time dependence is assumed to be a Ricker wavelet with a characteristic frequency of 500 Hz. A set of snapshots taken from computer animations is presented to illustrate the resulting wave field in the vicinity of both the acoustic barrier and dome at different time instants.

The system is subjected to a pressure pulse, with a characteristic frequency of 500.0 Hz, which starts acting at t=0 s. Fig. 8 shows contour plots of the pressure field at different time instants when the waves propagate in the vicinity of the acoustic barrier. In the plots red represents the higher pressure amplitudes and blue the lower ones.

In the first plots, at t=0.31 ms, the incident pulse is visible and propagating away from the source point without perturbations as it has not yet reached the ground and the acoustic barrier. As expected, the magnitude of the pressures is uniform along the cylindrical wavefronts.

At t=3.05 ms the incident pulse has struck the rigid ground and a reflected pulse is already visible. At t=10.68 ms the incident pulse has just hit the acoustic barrier. The reflected pulse is still very close to the acoustic barrier. The result of the waves' diffraction at the top of the barrier can be seen at t=14.65 ms. At

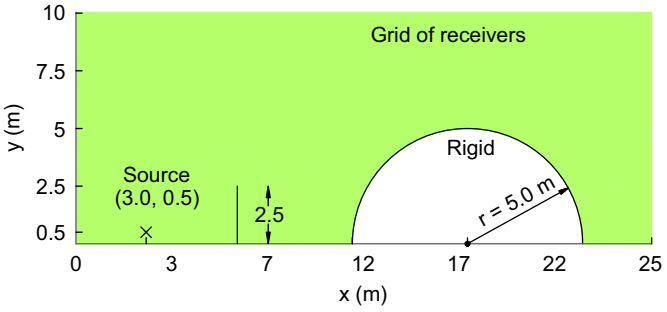

Fig. 6. Geometry of the rigid acoustic screen in the vicinity of a dome and position of the source and receivers.

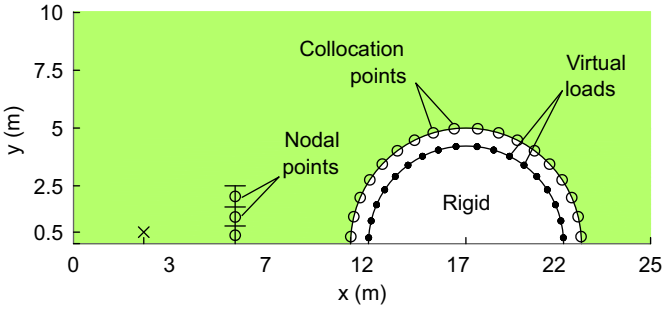

Fig. 7. Rigid acoustic screen in the vicinity of a dome: position of the virtual loads, collocation points and boundary elements.

t=18.01 and 21.06 ms the diffracted waves that originate at the top of the barrier can be seen travelling around the screen, while the incident and first reflected waves are reflected back at the barrier. At t=28.69 ms these waves are reflected on the ground, travelling upwards. As time passes the first set of reflections from the dome are visible (t=39.67 ms). The dome and the barrier are responsible for a set of multiple reflections, travelling back and forward between the two structures, shown in Fig. 8 (t=47.30 ms). In the last snapshot, these effects are more evident, and pulses trapped between rigid screens are visible in the response, particularly at receivers placed close to the ground (t=57.98 ms).

5.2. Thin acoustic barrier separating two railway tracks in an underground train station

Consider an underground station (air-filled), with two railway tracks, embedded in an unbounded acoustic medium (treated as fluid). A thin acoustic barrier (flat fluid-filled element) is placed inside the station to separate the two railway tracks. The scattered pressure field generated by the thin acoustic barrier, when excited by a harmonic point pressure load, is analyzed with the coupling (combined TBEM+BEM)/MFS formulation. In this problem, an acoustic point pressure load simulates the noise caused by a train and excites the same host medium described

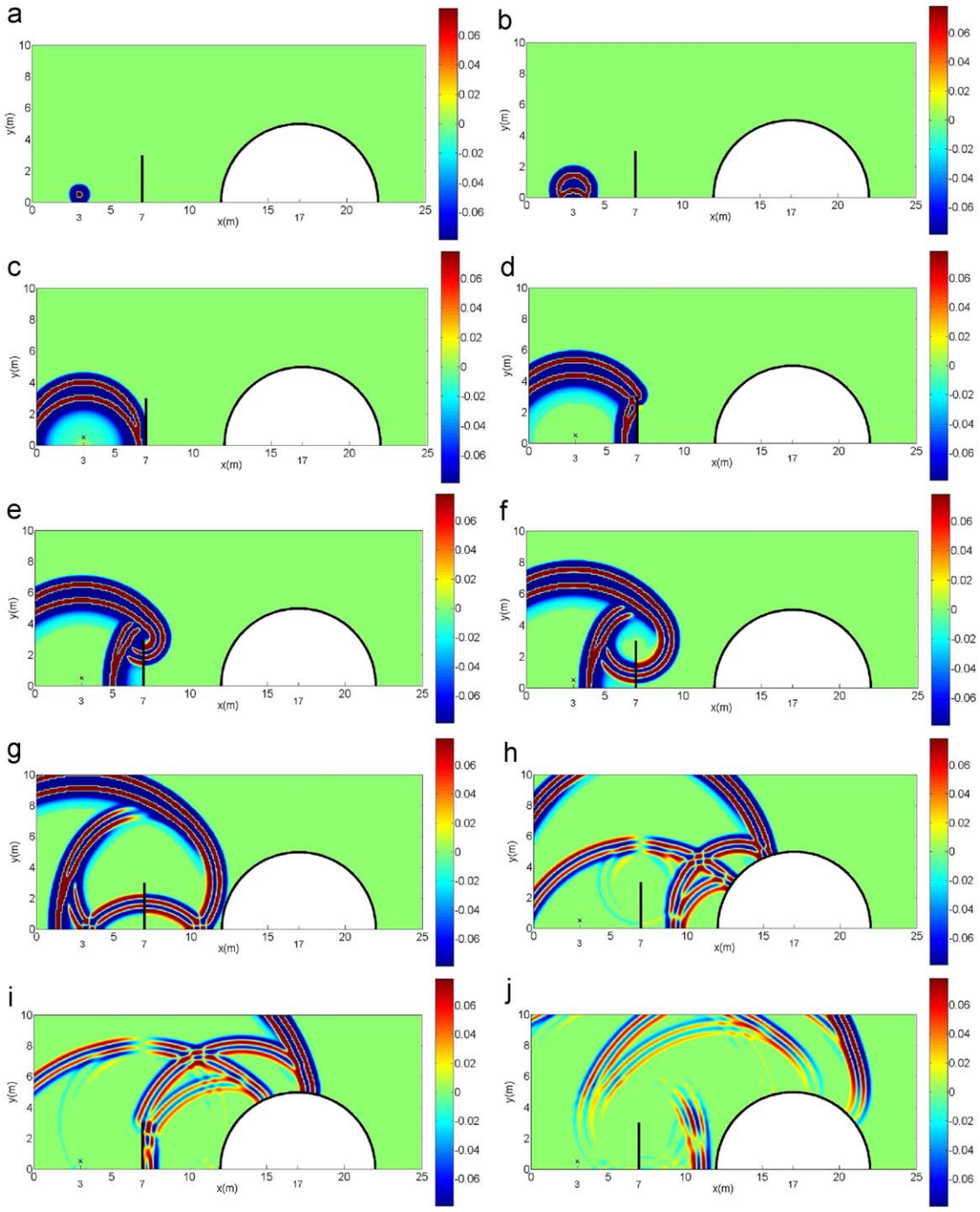

Fig. 8. Pressure wave propagation in the vicinity of an acoustic barrier and a dome. Time responses at t=0.31 ms (a), t=3.05 ms (b), t=10.68 ms (c), t=14.65 ms (d), t=18.01 ms (e), t=21.06 ms (f), t=28.69 ms (g), t=39.67 ms (h), t=47.301 ms (i) and t=57.98 ms (j).

before. A thin flat inclusion with rounded extremities is filled with a fluid with density 0.18 kg/m^3 and allowing a wave velocity of 360.0 m/s (these properties are identical to the density and dilatational P wave velocity of cork). The unbounded medium allows a pressure wave velocity of 2000.0 m/s and has a density of 1400.0 kg/m^3. As shown in Fig. 9, a cross-section view of the station, the thin acoustic barrier separates the two railway tracks, aiming to attenuate the noise produced by the neighboring train. The thin inclusion is 0.02 m thick and its extremities are defined by semi-circumferences. Part of the inclusion's surface is discretized by the TBEM formulation while the rest is discretized by the BEM. The surfaces of the underground station are modeled using the MFS. Fig. 10 shows the position of the virtual sources, collocation points and boundary elements. The virtual sources are placed 0.32 m from the metro station boundary. The same procedure as that described above was used to define the distance between the virtual sources and boundary. The selection of the number of virtual sources/collocation points was defined at each calculation frequency by the relation between the wavelength and distance between successive virtual sources/collocation points, and set at 6. The number of boundary elements was chosen by setting the relation between the wavelength and the length of the boundary elements at 6. A minimum of 700 collocation points/virtual sources and 240 boundary elements were used to discretize the metro station boundary and the acoustic barrier, respectively.

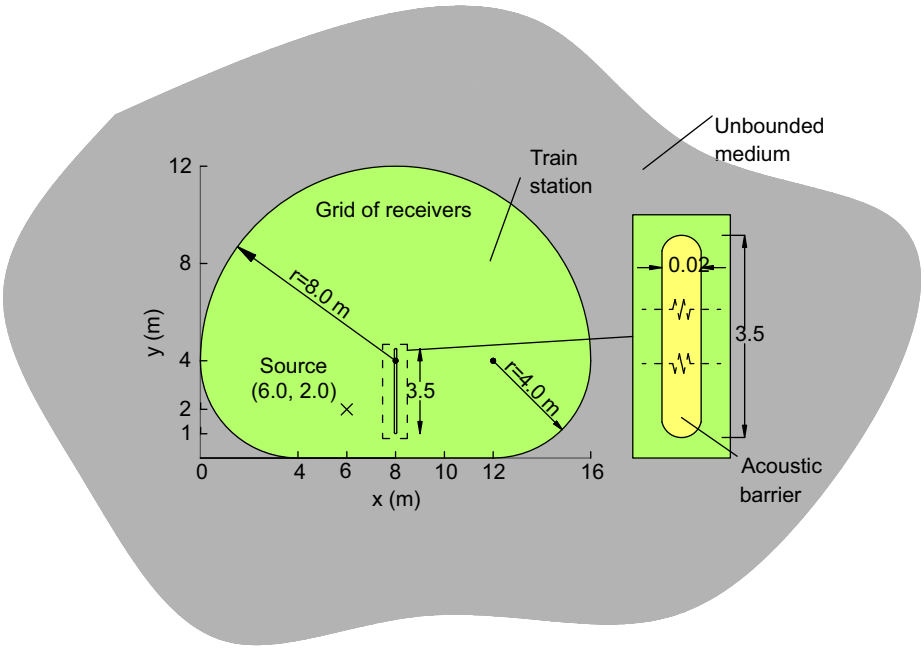

Fig. 9. Geometry of a thin acoustic barrier in an underground train station and position of the source.

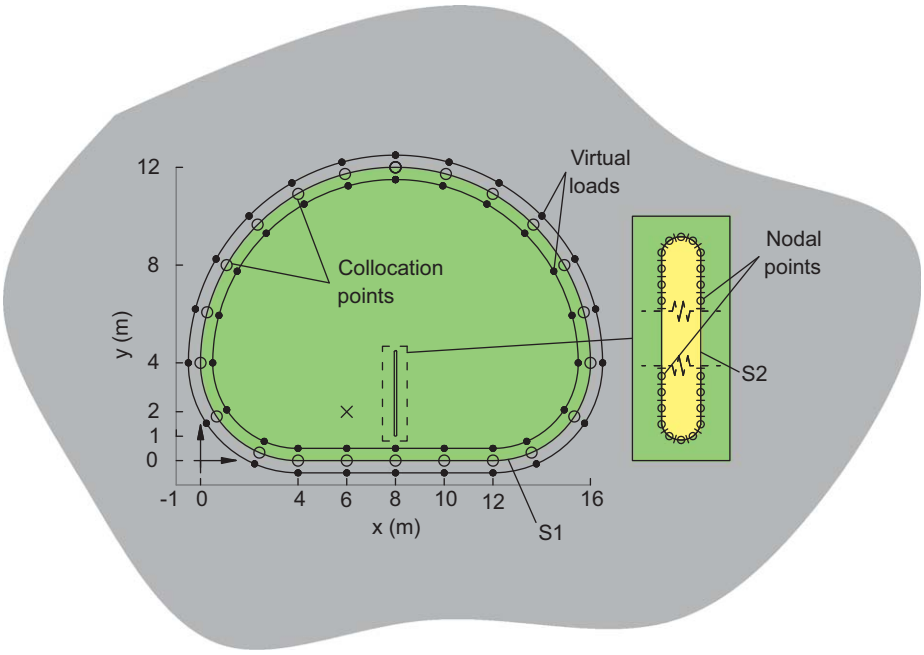

Fig. 10. Thin acoustic barrier in an underground train station: position of the virtual sources, collocation points and boundary elements.

Results were computed at a semi-circular grid of 4867 receivers equally spaced. The numerical results are presented in two-dimensional views at different time instants (Fig. 11), with color scale plots representing the total pressure field when the source is assumed to be modeled as a Ricker wavelet with a characteristic frequency of 400 Hz.

In the first plot, at $t=0.73$ ms, the pressure wave is propagating in the host fluid medium before reaching the flat thin inclusion, at $t=4.39$ ms. When it hits the fluid-filled inclusion the pressure incident field is partly reflected back, but part of it passes through the thin element ($t=8.54$ ms). In addition, diffracted waves are observable at the bottom of the barrier. Only a very small

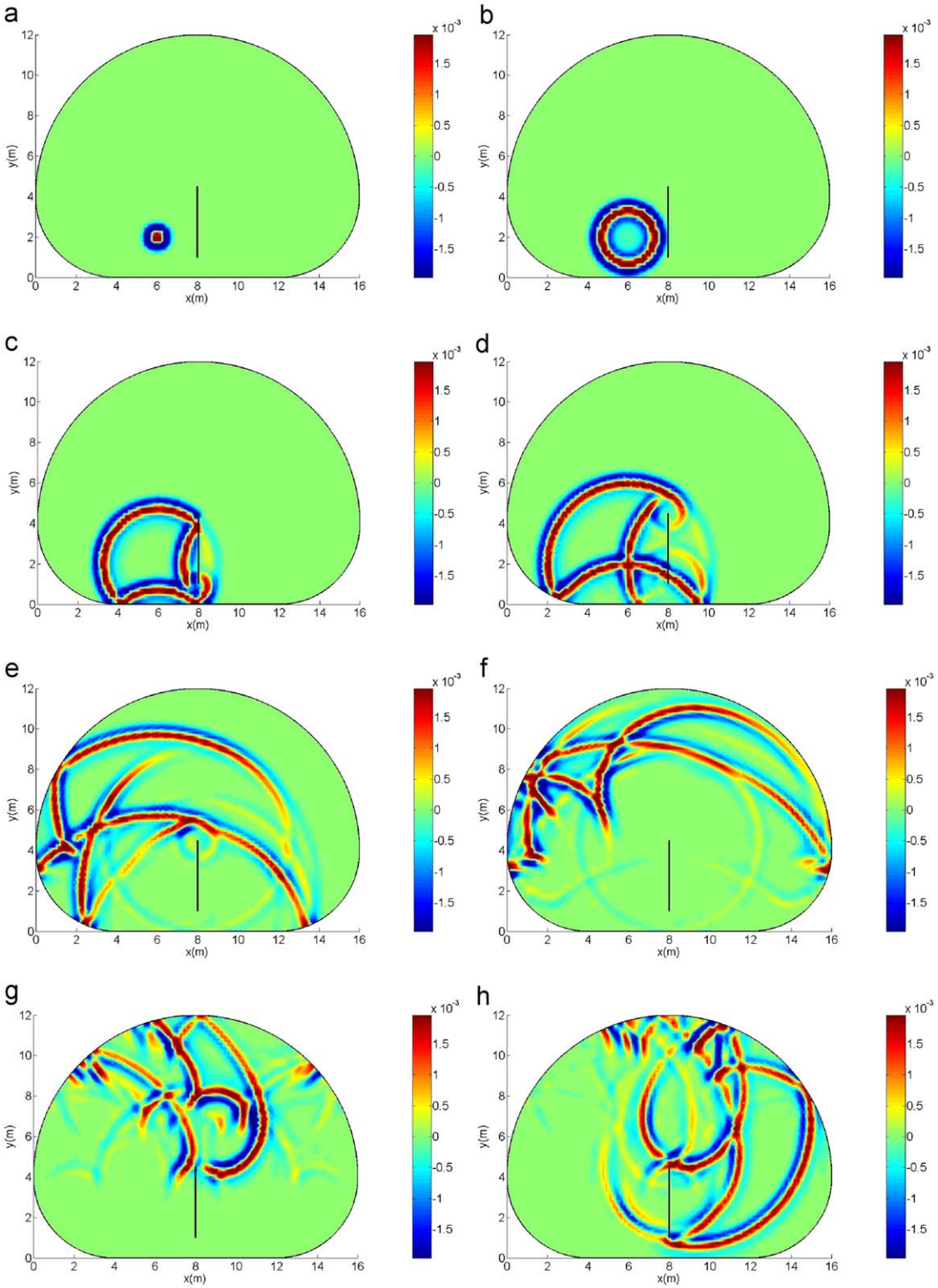

Fig. 11. Thin acoustic barrier separating two railway tracks in an underground train station. (a) Pressure field at $t=0.73$ ms; (b) pressure field at $t=4.39$ ms; (c) pressure field at $t=8.54$ ms; (d) pressure field at $t=12.21$ ms; (e) pressure field at $t=23.19$ ms; (f) pressure field at $t=33.69$ ms; (g) pressure field at $t=53.71$ ms; (h) pressure field at $t=63.96$ ms.

perturbation is observed as the pressure wave increases in a thin inclusion filled with a fluid different from the host medium. At t=12.21 ms the wave component that passed through the inclusion has already reached the right grid of receivers as it propagates away from the source position. The interference between these waves and those diffracted at the top and bottom of the barrier can be seen. The propagation of the reflected wave leftwards and some diffraction patterns generated by the incident acoustic field are clearly shown (see Fig. 11 e,f). Most of the reflected and transmitted pulses rise to the upper surface of the train station (t=53.71 ms), moving then to the right part of the grid, in last snapshot (t=63.96 ms). The dynamic process carries on with waves being reflected, diffracted and refracted at the boundaries of the barrier and of the train station walls until all the energy is dissipated.

6. Conclusions

The coupling between boundary element method (BEM)/ traction boundary element method (TBEM) and the method of fundamental solutions (MFS) has been proposed for the transient analysis of acoustic wave propagation problems in the presence of multi-inclusions. It was demonstrated that the proposed coupling algorithms overcome limitations posed by each method. They require less computational power while maintaining adequate accuracy.

The TBEM, and a combined formulation that uses both the TBEM and the classical BEM, coupled with the MFS, was proposed to overcome the thin-body difficulty. Problems involving thin heterogeneities which can be rigid, free or fluid-filled, in an unbounded or half-space homogeneous fluid medium that contains other inclusions, have been successfully addressed in this paper. The proposed coupling formulations were corroborated by comparing their solutions, and seen to closely follow the behavior of the conventional direct BEM or MFS solutions.

Finally, the proposed coupling formulations were used to solve two numerical examples. The propagation of two-dimensional pressure waves in the vicinity of a dome when a null-thickness rigid acoustic screen is placed between this structure and an acoustic source was addressed in the first example. In the second example, the attenuation of a pressure field produced by an acoustic source in the presence of a thin acoustic screen (seen as a fluid-filled thin inclusion) placed in a train station was computed to illustrate the capabilities of the proposed techniques.

Acknowledgment

The research work presented herein was supported by the Portuguese Foundation for Science and Technology (FCT), under the Grant SFRH/BD/37425/2007.

References

[1] Kausel E. Thin-layer method: formulation in the time domain. International Journal for Numerical Methods in Engineering 1994;37(6):927–41.
[2] Wu TW, editor. Southampton: WIT Press; 2000.
[3] Ihlenburg F, Germanischer L. Finite element analysis of acoustic scattering (Applied Mathematical Sciences). Springer; 1998.
[4] Thompson LL. A review of finite-element methods for time-harmonic acoustics. The Journal of the Acoustical Society of America 2006;119(3): 1315–30.
[5] Savioja L, Rinne T, Takala T. Simulation of room acoustics with a 3-D finite difference mesh. Proc ICMC'94, Aarhus, Denmark, 1994; 463–466.
[6] Kulowski A. Algorithmic representation of the ray tracing technique. Applied Acoustics 1985;18:449–69.
[7] Dell'erba DN, Aliabadi MH, Rooke DP. Dual boundary element method for three-dimensional thermoelastic crack problems. International Journal Fracture 1998;94:89–101.
[8] Rudolphi TJ. The use of simple solutions in the regularisation of hypersingular boundary integral equations. Mathematical and Computer Modelling 1991;15:269–78.
[9] Watson JO. Hermitian cubic boundary elements for plane problems of fracture mechanics. International Journal for Structural Mechanics and Material Science 1982;4:23–42.
[10] Watson JO. Singular boundary elements for the analysis of cracks in plane strain. International Journal of Numerical Methods in Engineering 1995;38:2389–411.
[11] Amado Mendes P, Tadeu A. Wave propagation in the presence of empty cracks in an elastic medium. Computational Mechanics 2006;38(3):183–99.
[12] Prosper D, Kausel E. Wave scattering by cracks in laminated media. Proc. of the Int. Conf. on Computational Engineering and Science ICES'01, Puerto Vallarta, Mexico; 2001.
[13] Tadeu A, Amado Mendes P, António J. 3D elastic wave propagation modelling in the presence of 2D fluid-filled thin inclusions. Engineering Analysis with Boundary Elements 2006;30(3):176–93.
[14] Tadeu A, Amado Mendes P, António J. The simulation of 3D elastic scattering produced by thin rigid inclusions using the traction boundary element method. Computers and Structures 2006;84(31–32):2244–53.
[15] Tadeu A, António J, Amado Mendes P, Godinho L. Sound pressure level attenuation provided by thin rigid screens coupled to tall buildings. Journal of Sound and Vibration 2007;304(3–5):479–96.
[16] António J, Tadeu A, Amado Mendes P. A 2.5D traction boundary element method formulation applied to the study of wave propagation in a fluid layer hosting a thin rigid body. Journal of Computational Acoustics 2007;16(2):177–98.
[17] Fairweather G, Karageorghis A. The method of fundamental solutions for elliptic boundary value problems. Advances in Computational Mathematics 1998;9:69–95.
[18] Fairweather G, Karageorghis A, Martin PA. The method of fundamental solutions for scattering and radiation problems. Engineering Analysis with Boundary Elements 2003;27:759–69.
[19] Chen JT, Chang MH, Chen KH, Chen IL. Boundary collocation method for acoustic eigenanalysis of three-dimensional cavities using radial basis function. Computational Mechanics 2002;29:392–408.
[20] Song K, Zhang X, Lu M. Meshless method based on collocation with consistent compactly supported radial basis functions. Acta Mechanica Sinica 2004;20(5):551–7.
[21] Smyrlis Y-S. The method of fundamental solutions: a weighted least-squares approach. BIT 2006;46:163–94.
[22] Brown D, Ling L, Kansa E, Levesley J. On approximate cardinal preconditioning methods for solving PDEs with radial basis functions. Engineering Analysis with Boundary Elements 2005;29:343–53.
[23] Godinho L, Tadeu A, Simões NA. Accuracy of the MFS and BEM on the analysis of acoustic wave propagation and heat conduction problems. In: Sladek Jan, Sladek Vladimir, editors. Advances in Meshless Methods. Tech Science Press; 2006.
[24] Godinho L, Tadeu A, Amado Mendes P. Wave propagation around thin structures using the MFS. Computers Materials and Continua 2007;5:117–28.
[25] Godinho L, Amado Mendes P, Tadeu A, Cadena-Isaza A, Smerzini C, Sánchez-Sesma FJ, et al. Numerical simulation of ground rotations along 2D topographical profiles under the incidence of elastic plane waves. Bulletin of the Seismological Society of America 2009;99(2B):1147–61.
[26] Alves CJS, Leitão VMA. Crack analysis using an enriched MFS domain decomposition technique. Engineering Analysis with Boundary Elements 2006;30(3):160–6.
[27] Manolis GD, Beskos DE. Boundary Element Methods in Elastodynamics. London: Unwin Hyman (sold to Chapman and Hall); 1988.
[28] Tadeu A, Santos P, Kausel E. Closed-form integration of singular terms for constant, linear and quadratic boundary elements. Part I. SH wave propagation. Engineering Analysis with Boundary Elements 1999;23(8): 671–681.
[29] Tadeu A, Amado Mendes P, António J. 3D elastic wave propagation modelling in the presence of 2D fluid-filled thin inclusions. Engineering Analysis with Boundary Elements 2006;30(3):176–93.
[30] Guiggiani M. Formulation and numerical treatment of boundary integral equations with hypersingular kernels. In: Sladek V, Sladek J, editors. Singular Integrals in Boundary Element Methods. Southampton and Boston: Computational Mechanics Publications; 1998.